

Discovery and origins of giant optical nebulae surrounding PKS0454–22

Jakob M. Helton,¹[★] Sean D. Johnson,^{1,2}[†] Jenny E. Greene¹

¹*Department of Astrophysical Sciences, 4 Ivy Lane, Princeton University, Princeton, NJ 08544, USA*

²*The Observatories of the Carnegie Institution for Science, 813 Santa Barbara Street, Pasadena, CA 91101, USA*

Accepted XXX. Received YYY; in original form ZZZ

ABSTRACT

The importance of galaxy environment and interactions in dictating the gas flows that fuel both galaxy and black hole growth remains an important, unresolved problem of extragalactic astrophysics. We report optical integral-field spectroscopy of one of the most luminous quasars in the $z < 1$ Universe, PKS0454–22, at a redshift of $z_{\text{QSO}} = 0.5335$ with the Multi-Unit Spectroscopic Explorer at the Very Large Telescope. These data enable the discovery of three spatially extended ionized nebulae emitting strongly in [O II], H β , and [O III] on scales of 10 – 150 pkpc in the quasar host group. One of these nebulae spatially and kinematically surrounds the quasar host and a nearby galaxy on scales of 10 – 75 pkpc. The morphology and kinematics of this nebula are most consistent with stripped interstellar medium resulting from ongoing interactions between galaxies and the quasar host group. The ionization properties of this nebula can be explained solely with quasar photoionization. Another of these nebulae extends over 75 pkpc while spatially and kinematically surrounding a distinct association of three galaxies which are $d \approx 90$ pkpc and $\Delta v \approx 1320$ km s^{–1} from the quasar host. The morphology and kinematics of this nebula are also consistent with stripped interstellar medium resulting from ongoing interactions. However, the high ionization state of this nebula requires additional ionization sources beyond the quasar, likely the result of fast shocks as it moves through the hot halo of the quasar host group. The third and smallest of these nebulae is 25 pkpc in spatial extent and arises $d \approx 75$ pkpc from the quasar. It is not spatially or kinematically coincident with any detected galaxies and likely arises from a cool gas structure in the intragroup medium. The presence of these spatially extended ionized nebulae in the host group of one of the most luminous quasars in the $z < 1$ Universe provide evidence supporting interaction related triggering of quasars. Interactions such as these also drive large quantities of interstellar medium to the circumgalactic medium, producing cool gas structures on halo scales. The growing archive of data and availability of wide-area integral field spectrographs will continue to be a powerful tool in revealing the morphologies, kinematics, and physical conditions of the gas flows which may fuel both galaxy and black hole growth.

Key words: galaxies: interactions – quasars: general – quasars: individual (PKS0454–22)

1 INTRODUCTION

Observations have found that supermassive black holes (SMBHs) are present at the centers of most galaxies today (Kormendy & Richstone 1995; Kormendy & Ho 2013). Despite the orders-of-magnitude difference in spatial scale, the masses of SMBHs are tightly correlated with various

properties of their host galaxy, including the stellar velocity dispersion (Gebhardt et al. 2000; Tremaine et al. 2002) and the spheroid mass (McLure & Dunlop 2002; Häring & Rix 2004). These tight correlations suggest that SMBHs and galaxy spheroids are formed through a common process. Understanding the physical origins of these relations and their connection to galaxy evolution remains an important, unresolved goal of extragalactic astrophysics.

There are a number of related physical processes that may play a role in establishing the observed correlations be-

[★] E-mail: jhelton@princeton.edu

[†] Corresponding author; E-mail: sdj@astro.princeton.edu

tween SMBHs and their hosts. These include: (1) feedback from actively accreting SMBHs (AGN), (2) common fueling mechanisms, (3) interactions/mergers, and/or (4) galactic environment. The radiative and mechanical feedback processes associated with AGN can establish the observed correlations between SMBHs and their hosts by removing or heating gas, thus truncating both star formation and black hole growth. Because of this, AGN and their profound energy output have become a crucial part of modern galaxy formation theories (for a review, see [Somerville & Davé 2015](#)).

The observed correlations between SMBHs and their hosts can also be explained by common fueling mechanisms, which may be facilitated by interactions/mergers and galactic environment ([Peng 2007](#); [Jahnke & Macciò 2011](#)). In particular, fueling nuclear activity requires a redistribution of angular momentum in the interstellar medium (ISM), which allows sufficient gas to infall towards the nucleus ([Stockton 1978](#); [Yee & Green 1984, 1987](#); [Smith & Heckman 1990](#); [Bahcall & Chokshi 1991](#); [Bahcall et al. 1997](#); [Di Matteo et al. 2003](#); [Springel et al. 2005](#); [Somerville et al. 2008](#)). While gas-rich galaxy-galaxy interactions/mergers are capable of fueling black hole growth ([Barnes & Hernquist 1996](#); [Hopkins & Quataert 2010](#)), simulations suggest that their efficacy depends on the host galaxy’s environment ([Hopkins et al. 2006, 2008a](#); [Hopkins et al. 2008b](#)). Additionally, observational evidence indicates that black hole growth is most common in overdense galactic regions, such as small groups or clusters, where mergers may be most efficient ([Hickox et al. 2009](#); [Stott et al. 2020](#)).

In recent years, both observations ([Myers et al. 2007a,b](#); [Ross et al. 2009](#); [Shen et al. 2007](#); [White et al. 2012](#)) and theoretical modeling ([Hopkins et al. 2006, 2008a](#); [Hopkins et al. 2008b](#)) have shown that AGN are most common in small to intermediate mass groups. There are a few reasons why this characteristic scale may occur. First, a major merger is generally required to redistribute angular momentum and allow ISM to infall toward the nucleus during a sufficiently short time period ([Martini 2004](#)). Second, the galaxies involved in this major merger must contain sufficient gas supplies ([Hernquist 1989](#); [Barnes & Hernquist 1991, 1996](#)). Together, these two effects cause the characteristic halo mass for gas-rich galaxy-galaxy interactions/mergers, and possibly fueling of the most powerful AGN (quasars; with $L_{\text{bol}} > 10^{45} \text{ erg s}^{-1}$), to occur in galaxy groups.

Understanding the roles of mergers, star formation, and feedback in the coevolution of SMBHs and galaxies requires knowledge of where the gas is located. At $z = 0$, deep 21-cm emission reveal the gas locations and kinematics of even diffuse, extended gas (for a review, see [Duc & Renaud 2013](#)), but there are almost no luminous quasars to observe at such low redshifts. At $z \gg 0$, there are many luminous quasar to observe, but 21-cm observations of diffuse gas at these redshifts is not currently possible. However, luminous quasars and shocks are able to photoionize the denser phases of the circumgalactic medium (CGM), allowing gas which is normally neutral to emit strongly in the rest optical and ultraviolet (UV) ([Cantalupo et al. 2014](#); [Borisova et al. 2016](#); [Epinat et al. 2018](#); [Johnson et al. 2018](#); [Chen et al. 2019](#)). Thus, photoionization from quasars and shocks can push observations of extended gas in emission to $z \gg 0$ by allowing typically unobservable gas to emit strongly in ionized emission lines.

Combining this photoionization of large-scale gas supplies with the use of wide-field integral field spectroscopy (IFS) can provide a powerful means of simultaneously surveying the galactic and gaseous environments of quasars. This combination allows both sensitive searches for extended line-emitting nebulae and joint studies of their morphologies and kinematics in the context of those of nearby galaxies. Analysis of this information gives studies the ability to determine the properties of quasar host environments, explain the origin of luminous quasars, and improve upon modern galaxy formation theories through a better understanding of the relationship between group environment, large-scale gas supplies, and the evolution of both galaxies and AGN ([Husemann et al. 2010, 2016](#); [Johnson et al. 2018](#); [Chen et al. 2019](#)).

In this paper, we present the discovery of ionized nebulae emitting strongly in [O II], $H\beta$, and [O III] on scales of $10 - 150 \text{ pkpc}$ in the environment of one of the most luminous quasars in the $z < 1$ Universe, PKS0454–22, using IFS. Joint analyses of the morphologies and kinematics of these nebulae, and galaxies in the quasar host group, show that these nebulae arise from ongoing interactions and cool clouds in the intragroup medium (IGrM) rather than large-scale outflows ($\gtrsim 10 \text{ pkpc}$), which is typically assumed ([Yuma et al. 2013](#)). These observations provide important insights into the relationship between quasar fueling, gas-rich galaxy-galaxy interactions/mergers, and large-scale gas supplies.

This paper proceeds as follows. In Section 2, we describe the various measurements and observations of PKS0454–22. In Section 3, we present the galactic and nebular environments of this system. In Section 4, we discuss the origin of the observed nebular photoionization and gas. In Section 5, we conclude with the implications of our findings. All magnitudes are in the AB system, unless otherwise stated. Throughout the paper, we adopt a standard flat Λ CDM cosmology with $\Omega_m = 0.3$, $\Omega_\Lambda = 0.7$, and $H_0 = 70 \text{ km s}^{-1} \text{ Mpc}^{-1}$.

2 OBSERVATIONS AND MEASUREMENTS

2.1 The Multi-Unit Spectroscopic Explorer

Observations by the Multi-Unit Spectroscopic Explorer (MUSE; [Bacon et al. 2010, 2014](#)) of PKS0454–22 were obtained on January 23, 2018 as part of a European Southern Observatory (ESO) Very Large Telescope (VLT) program (PI: C. Peroux, PID: 0100.A-0753) to study the galactic environments of foreground intergalactic medium (IGM) absorption systems at $z \approx 0.27 - 0.48$, identified in the UV spectra of the quasar ([Peroux et al. 2019](#)). The program obtained a total science exposure time of 2700s under good conditions with median full width at half maximum seeing (FWHM) of 0.6 arcsec . They split the observations into four individual science exposures with standard dithering and rotation to minimize cosmic rays and artifacts as well as to suppress flat-fielding residuals in the final combined datacube.

MUSE is an optical integral-field spectrograph (IFS) on the VLT UT4 that captures a $1.0 \text{ arcmin} \times 1.0 \text{ arcmin}$ field of view (FOV) with a spatial sampling of $0.2 \text{ arcsec} \times 0.2 \text{ arcsec}$ spaxels in wide-field mode. Spectrally, MUSE has a contiguous wavelength range of $4750 - 9350 \text{ \AA}$ and resolution of $R \sim 2000 - 4000$, with higher resolution at the red end.

The combination of wide FOV, high spatial sampling, and broad wavelength coverage of MUSE provide an ideal and serendipitous opportunity to study the gaseous and group environment hosting PKS0454–22.

To study the environment of PKS0454–22 we obtained the publicly-available, reduced MUSE datacube of PKS0454–22 from the ESO Science Archive Facility. In summary, the ESO MUSE reduction pipeline performs bias subtraction, flat fielding, wavelength calibration, and geometric calibration (Weilbacher et al. 2012). All four exposures were reduced independently and then combined to create the final datacube with drizzle resampling. During this step, the data is also flux calibrated and sky subtracted based on regions free of continuum sources.

2.2 Quasar Measurements and Inferred Properties

While PKS0454–22 is a well studied luminous, radio-loud, jetted quasar (Reid et al. 1999), the MUSE data offer a new opportunity to examine the spectroscopic properties of the AGN. For PKS0454–22, we extracted a 1D MUSE spectrum using MPDAF with a 1.2 arcsec aperture diameter, chosen to be twice the median seeing of the MUSE datacube. We then measured the redshift from the [O II] $\lambda\lambda 3727, 3729$ emission line doublet with Gaussian fitting. The best-fit redshift of the quasar is $z_{\text{QSO}} = 0.5335 \pm 0.0002$.

To better understand the intrinsic properties of PKS0454–22 and aid in subsequent photoionization analysis, we also estimated the central black hole mass, bolometric luminosity, and inferred Eddington ratio, following the prescription of Vestergaard & Peterson (2006a). We fit the extracted quasar spectrum with a power-law function as the primary continuum, a broadened FeII template spectrum as the secondary continuum (Boroson & Green 1992; Vestergaard & Wilkes 2001), and multiple Gaussian line profiles as the emission lines. Prominent broad-line emission is seen in H γ and H β , with three broad Gaussian line profiles being necessary to model these lines. Prominent narrow-line emission is seen in H γ , H β , and [O III] $\lambda\lambda 4959, 5008$, with two narrow Gaussian line profiles being necessary to model these lines. We inferred a continuum luminosity at 5100 Å (rest frame) of $L_{5100} \approx 10^{46}$ erg s $^{-1}$ and a bolometric luminosity of $L_{\text{bol}} \approx 10^{47}$ erg s $^{-1}$, with bolometric corrections from Richards et al. (2006). Using an empirical relationship between the line width of the H β broad component and optical continuum luminosity, calibrated with mass measurements of local AGN based on emission line reverberation mapping (Vestergaard & Peterson 2006b), we estimate a fiducial virial mass from H β . We inferred a central black hole mass of $M_{\text{bh}} \approx 4 \times 10^9 M_{\odot}$. Together, the bolometric luminosity and central black hole mass give an inferred Eddington ratio of $\lambda \approx 0.16$. The quasar spectrum used to make these measurements is shown in the top panel of Figure 2.

2.3 Quasar Light Subtraction

PKS0454–22 is a bright quasar with $V \approx 16$ mag resulting in significant contamination of sources within $\lesssim 6$ arcsec from the quasar due to broad wings on the MUSE point-spread function (PSF), even under good seeing conditions. To remove this contaminating flux, we developed a quasar light

subtraction technique that is free of assumptions about the PSF shape, and instead takes advantage of the spectral dimension provided by an IFS and the fact that galaxy and quasar spectra are distinct. One problem with this approach is the wavelength dependence of the PSF, which disperses blue light further away from the quasar centroid than red light, resulting in an artificially flat quasar spectrum close to the quasar and an artificially steep quasar spectrum far from the quasar (Rupke et al. 2017). We used non-negative matrix factorization (NMF) to account for this (Blanton & Roweis 2007; Ren et al. 2018), which is described in detail in the appendix and summarized here. In this case, we determined the two non-negative spectral components that can best model the quasar contribution to any spaxel as linear combinations by performing NMF on quasar-dominated spaxels from a $1.0 \text{ arcsec} \times 1.0 \text{ arcsec}$ aperture centered around the quasar. We modeled each spaxel at $\lesssim 6$ arcsec from the quasar as a linear combination of two quasar components and two Sloan Digital Sky Survey (SDSS) galaxy eigenspectra from the Baryon Oscillation Spectroscopic Survey (BOSS) shifted to $z_{\text{QSO}} = 0.5335$ with the strongest emission lines masked (Bolton et al. 2012). We then subtracted the quasar component of the best-fit model from each spaxel, which removes the quasar light contribution at $\gtrsim 1$ arcsec from the quasar (Johnson et al. 2018). At $\lesssim 1$ arcsec from the quasar centroid, the residuals are significant as seen in Figure A2, so we masked this region in subsequent analysis.

2.4 Galaxy Detection and Redshift Measurements

After quasar light subtraction, we identified continuum sources in the field of PKS0454–22 with Source Extractor (Bertin & Arnouts 1996). To do this, we used both a white-light image created from the MUSE datacube with spectral coverage of 6250 – 7250 Å (free of strong emission lines at $z_{\text{QSO}} = 0.5335$) and an archival image from the Wide Field and Planetary Camera 2 (WFPC2) on the *Hubble Space Telescope* (HST) with the F702W filter and total integration time of 4800s (PI: K. Lanzetta, PID: 7475). Figure 1 shows a $60 \text{ arcsec} \times 60 \text{ arcsec}$ cutout of the HST WFPC2+F702W image of the field with group members labeled, matching the $60 \text{ arcsec} \times 60 \text{ arcsec}$ MUSE FOV. The resulting continuum source catalog is complete at $m_{\text{F702W}} \approx 25\text{--}26$ based on background sky estimation from the image of the field and the HST WFPC2+F702W exposure time calculator.

For each detected continuum source, we extracted the corresponding 1D MUSE spectrum using MPDAF (Piqueras et al. 2017) with aperture diameters determined by Source Extractor. These aperture diameters represent the minimum spatial root mean square (rms) dispersion of the object profile along any direction. We then measured the redshift of each source by determining the best-fit redshift using SDSS galaxy eigenspectra from BOSS. At each redshift on a grid from $z = 0.0$ to $z = 1.0$ with steps of $\Delta z = 0.0001$, we fit the observed spectrum with a linear combination of the SDSS eigenspectra. We adopted the global minimum- χ^2 solution as our initial redshift measurement, visually inspected the resulting χ^2 grid, and compared the observed spectrum to the best fit in order to judge redshift measurement quality. To ensure robust redshift measurements, we required at least two distinct observed spectral features to be fit properly. The resulting galaxy redshift uncertainties are $v \approx 20 \text{ km s}^{-1}$.

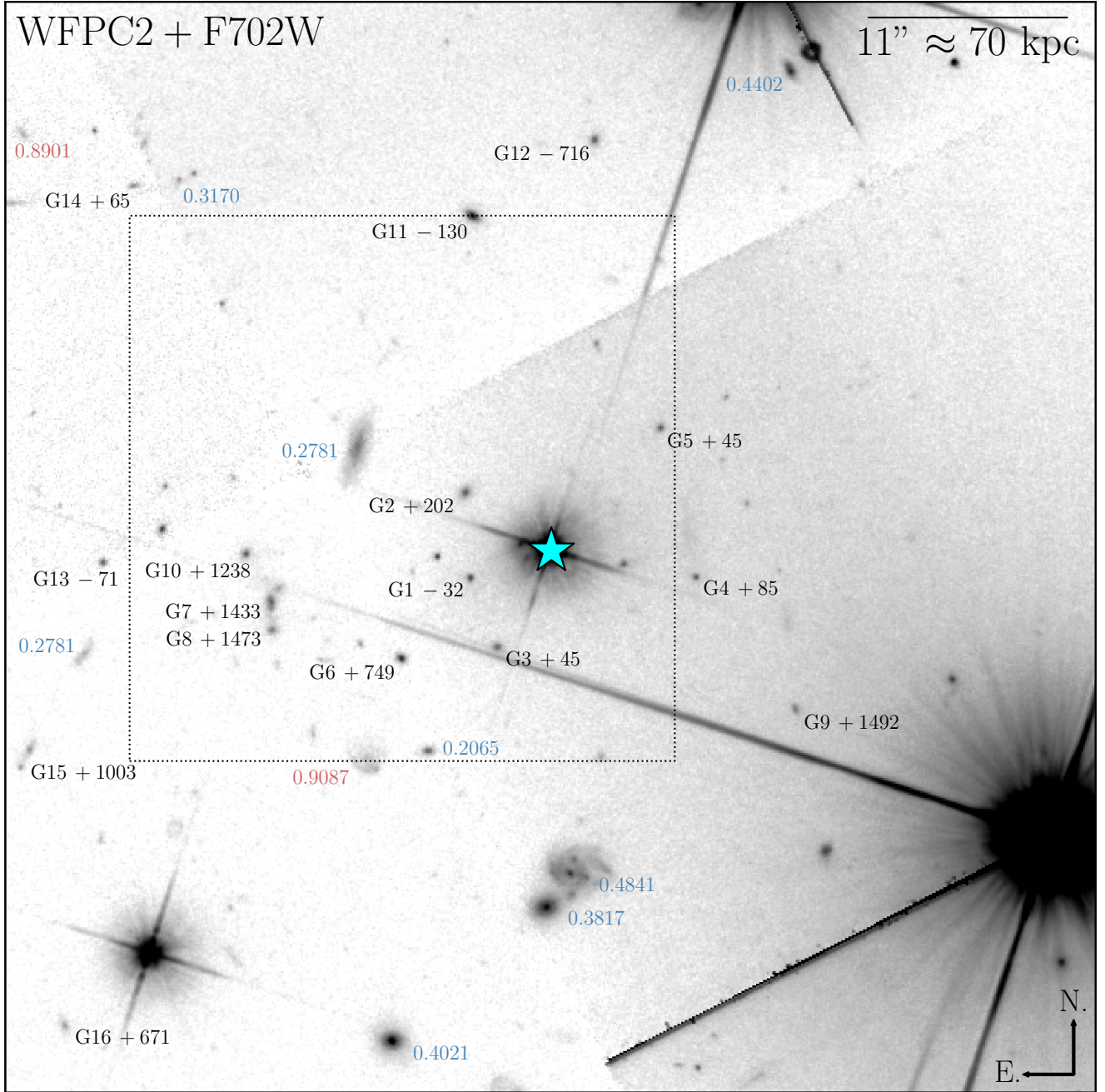


Figure 1. *HST* WFPC2+F702W image of the field of PKS0454-22. Galaxies in the quasar host group are labeled by their ID and LOS velocity from the quasar in km s^{-1} ($z_{\text{QSO}} = 0.5335$). Galaxies that are foreground to the group are labeled with smaller font by their redshift in blue, while galaxies that are background to the group are labeled in red. The quasar is marked by a cyan star. The full image shows the 60 arcsec \times 60 arcsec MUSE FOV and the dotted box marks the 30 arcsec \times 30 arcsec region displayed in Figure 4.

Figure 2 shows examples of co-added galactic spectra and the best-fitting spectral models used for redshift measurements. The survey remains approximately 100% complete at observed-frame apparent magnitude with the F702W filter on *HST* at $m_{\text{F702W}} \approx 23$ and approximately 90% complete at $m_{\text{F702W}} \approx 24$. The high completeness of the galaxy detection and redshift measurements enable a detailed investigation of possible environmental dependence of extended gas around galaxies.

3 THE ENVIRONMENT OF PKS0454-22

3.1 Galactic Environment

We identified candidate members of the quasar host environment by selecting galaxies with line-of-sight (LOS) velocities of $|\Delta v| < 2000 \text{ km s}^{-1}$ from the quasar. We chose this velocity range to be approximately twice the velocity dispersion of the most massive galaxy clusters. We identified 17 galaxies in the MUSE field within this velocity range, including

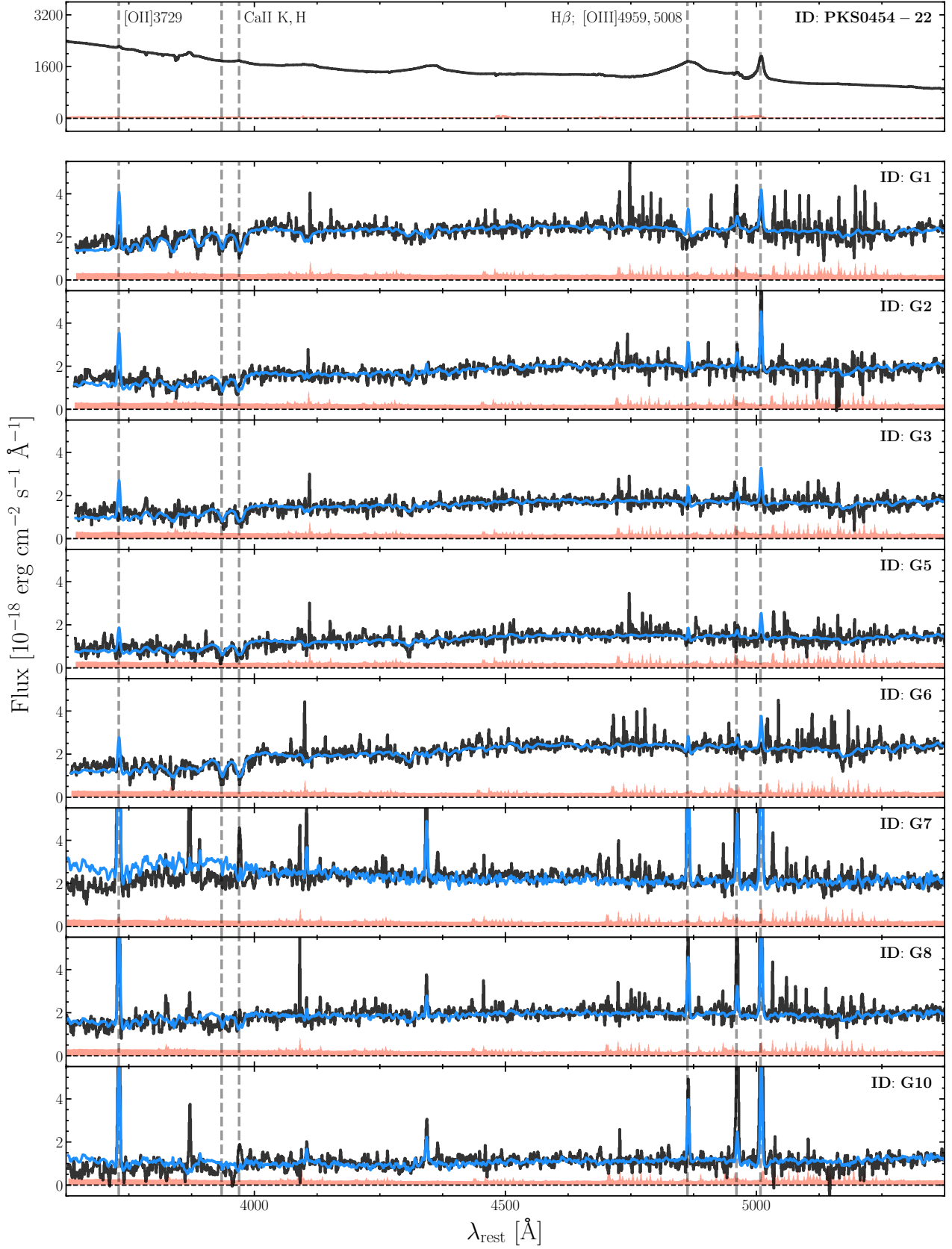


Figure 2. Examples of co-added galactic spectra and best-fitting spectral models for each of the 8 nearby galaxies present in the $30 \text{ arcsec} \times 30 \text{ arcsec}$ region displayed in Figure 4. The MUSE spectrum is shown by a solid line in black with errors shown by a filled area in red, while the best-fit spectral model is shown by a solid line in blue. This best-fit spectral model is solely used for redshift measurements. Galaxy labels are in the upper-right corner of each panel.

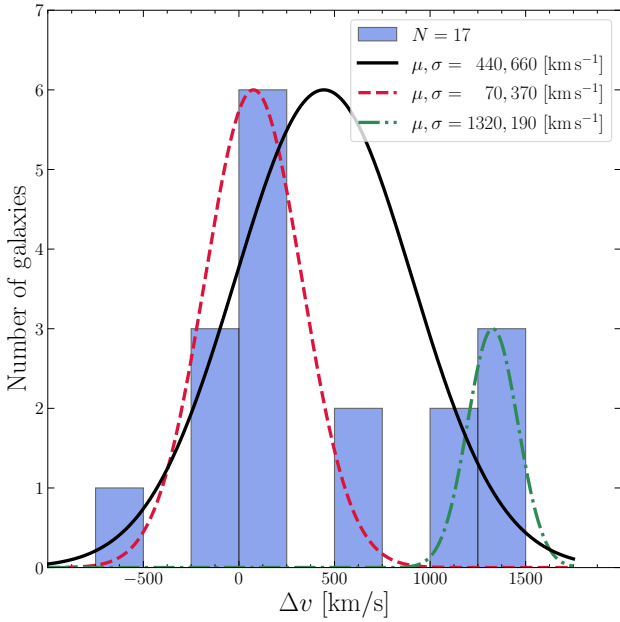


Figure 3. Histogram displaying the LOS velocity from the quasar ($\Delta v = v - v_{\text{QSO}}$) of galaxies in the galactic environment of PKS0454–22.

the quasar host. Some relevant physical properties of these galaxies are shown in Table 1.

The quasar host environment includes 8 (17) galaxies of $m_{\text{F702W}} \leq 23.5$ (24.0) suggesting a relatively massive group. Assuming all of these galaxies to be part of a single relaxed “group” and based on galaxies of $m_{\text{F702W}} \leq 24.0$, the mean velocity of these “group” members is $\Delta v_{\text{group}} \approx 440 \text{ km s}^{-1}$ from the quasar systemic velocity and the nominal velocity dispersion is $\sigma_{\text{group}} \approx 660 \text{ km s}^{-1}$. Not including the quasar, the light-weighted group center is 50.7 pkpc east and 3.0 pkpc south of the quasar. The distribution of galaxy LOS velocities relative to the quasar ($\Delta v = v - v_{\text{QSO}}$) is shown in Figure 3.

The galaxy LOS velocities relative to the quasar are characterized by two peaks at $\Delta v \approx 70 \text{ km s}^{-1}$ and $\Delta v \approx 1320 \text{ km s}^{-1}$. Galaxies in the $\Delta v \approx 70 \text{ km s}^{-1}$ peak are primarily located around the quasar while galaxies in the $\Delta v \approx 1320 \text{ km s}^{-1}$ peak are primarily located $d \approx 100$ pkpc east of the quasar. These kinematic and spatial bimodalities can be explained if perhaps the smaller group of 5 galaxies at $\Delta v \approx 1320 \text{ km s}^{-1}$ (with $\sigma \approx 190 \text{ km s}^{-1}$) is interacting with or infalling into the more massive quasar host group with 12 galaxies at $\Delta v \approx 70 \text{ km s}^{-1}$ (with $\sigma \approx 370 \text{ km s}^{-1}$). The light-weighted group center of the smaller group is 84.3 pkpc east and 29.2 pkpc south of the quasar while the light-weighted group center of the more massive quasar host group is 34.2 pkpc east and 18.8 pkpc south of the quasar.

To gain further insights into the galactic environment of PKS0454–22, we display a $30 \text{ arcsec} \times 30 \text{ arcsec}$ cutout of the *HST* WFPC2+F702W image with group members labeled in the top-left panel of Figure 4 and a $30 \text{ arcsec} \times 30 \text{ arcsec}$ cutout of the quasar light-subtracted MUSE image averaged over $6250 - 7250 \text{ \AA}$ (free of strong emission lines at $z_{\text{QSO}} = 0.5335$) in the top-middle panel of Figure 4. The galaxy

morphologies, projected separations, and relative velocities indicate that Host/G1/G2 are an interacting galaxy triple with a projected separation of 37.4 pkpc and G8/G7/G10 are an interacting galaxy triple with a projected separation of 25.7 pkpc. These interacting galaxies all exhibit relatively red rest-frame colors of $u-g = 0.5 - 0.7$, consistent with intermediate to old characteristic stellar populations (Strateva et al. 2001).

3.2 Nebular Environment

The MUSE data enable the discovery of 3 kinematically and morphologically distinct, ionized nebulae emitting strongly in [O II], $\text{H}\beta$, and [O III] on scales of $10 - 150$ pkpc and at LOS velocities of $\Delta v \approx -500$ to $+1500 \text{ km s}^{-1}$ from the quasar. Some relevant physical properties of these nebulae including size, luminosity, kinematics, and association with galaxies are shown in Table 2. Throughout, we refer to the nebulae by their size and total line luminosity, as labeled in the top-middle panel of Figure 4 and Table 2: Nebula 1 (N1), Nebula 2 (N2), and Nebula 3 (N3). Nebula 1 is morphologically coincident with Host/G1/G2, with $\Delta v \approx 140 \text{ km s}^{-1}$ and $\sigma \approx 140 \text{ km s}^{-1}$. Nebula 2 is morphologically coincident with G8/G7/G10, with $\Delta v \approx 1330 \text{ km s}^{-1}$ and $\sigma \approx 120 \text{ km s}^{-1}$. Nebula 3 is not morphologically coincident with any detected galaxies, with $\Delta v \approx 550 \text{ km s}^{-1}$ and $\sigma \approx 50 \text{ km s}^{-1}$.

To visualize the morphologies of these nebulae alongside galaxies in the group, we display [O III] emission contours over the quasar light-subtracted MUSE image averaged over $6250 - 7250 \text{ \AA}$ (free of strong emission lines at $z_{\text{QSO}} = 0.5335$) in the top-middle panel of Figure 4. To visualize the kinematics of these nebulae and their association with galaxies in the group, we display a LOS velocity map of the nebulae relative to the quasar in the top-right panel of Figure 4. Subsequent panels in Figure 4 display narrowband images extracted from the MUSE datacube at the observed-frame wavelength of [O III] over the given velocities, chosen to highlight each of the nebulae and reveal detailed structure.

For each nebula, we measured line luminosities; LOS velocities; and LOS velocity dispersions at each spaxel using a spectral modeling technique where the continuum is fit by a linear combination of two simple stellar population models with characteristic ages of 290 Myr and 5 Gyr (Bruzual & Charlot 2003), and emission lines are fit by a single set of Gaussian line profiles that are all coupled in their radial velocity and intrinsic velocity dispersion. We estimated standard errors from the MUSE error array and covariance matrix. Examples of co-added nebular spectra and best-fitting spectral models for various regions within each of the 3 kinematically and morphologically distinct, ionized nebulae (N1, N2, and N3) are shown in Figure 5 with two spectral windows: one covering [O II] $\lambda\lambda 3727, 3729$, and one covering $\text{H}\beta$ and [O III] $\lambda\lambda 4959, 5008$. In addition to these strong lines, we detect several fainter lines in the brightest nebular regions, such as [Ne V] $\lambda 3426$, [Ne III] $\lambda 3869$, $\text{H}\delta$, $\text{H}\gamma$, [O III] $\lambda 4363$, and $\text{He II} \lambda 4687$.

Within the closest nebula to PKS0454–22, we noticed a second peak blueward of the [O III] $\lambda\lambda 4959, 5008$ lines at a projected distance of 10.3 pkpc from the quasar. This blue peak is visible in the top panel of Figure 5, which displays

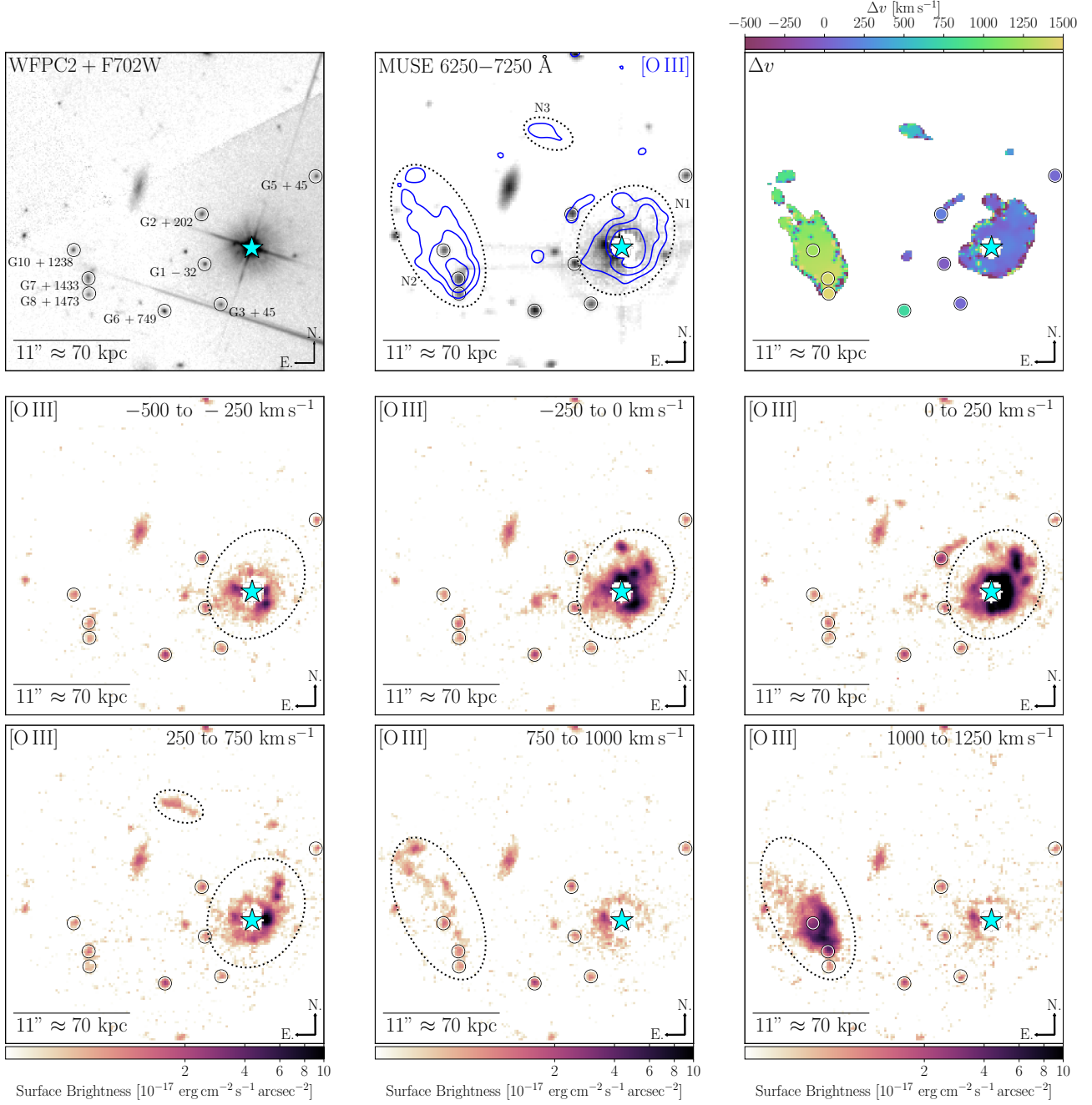


Figure 4. *Top-left panel:* *HST* WFPC2+F702W image of the field of PKS0454–22. The positions of galaxies in the host group are marked by circles and labeled by their IDs and LOS velocities relative to the quasar. *Top-middle panel:* median flux image over 6250–7250 Å in the MUSE datacube with [O III] surface brightness contours of 0.2, 0.8, and $3.2 \times 10^{-17} \text{ erg cm}^{-2} \text{ s}^{-1} \text{ arcsec}^{-2}$ in blue. Nebulae are marked by dashed ellipses and labeled by their IDs, the positions of galaxies in the host group are marked by circles, and the quasar is marked by a cyan star. *Top-right panel:* map of the nebular LOS velocities relative to the quasar, showing spaxels with significant detection of [O III] ($S/N > 3$). The positions of galaxies in the host group are marked by circles and the quasar is marked by a cyan star. *Middle row and bottom row:* narrow-band [O III] images extracted from the MUSE datacube over the LOS velocity intervals indicated in each panel. Nebulae are marked by dashed ellipses, the positions of galaxies in the host group are marked by circles, and the quasar is marked by a cyan star.

Table 1. Summary of Galaxies in the Field of PKS0454–22 at $z \approx z_{\text{QSO}}$.

ID	R.A. ^a (J2000)	Decl. ^b (J2000)	m_{F702W}^c (AB)	M_g^d (AB)	z^e	$u-g^f$ (AB)	$\Delta\theta^g$ (arcsec)	d^h (pkpc)	Δv^i (km s ⁻¹)
Host	04:56:08.90	-21:59:09.11	0.5335	...	0.0	0.0	0
G1	04:56:09.22	-21:59:10.88	23.2	-18.9	0.5333	0.6	5.1	32.5	-32
G2	04:56:09.23	-21:59:06.13	23.1	-19.0	0.5345	0.7	5.8	37.4	+202
G3	04:56:09.11	-21:59:14.58	23.7	-18.4	0.5337	0.7	6.3	40.5	+45
G4	04:56:08.34	-21:59:09.98	23.8	-18.3	0.5339	0.3	8.5	54.4	+85
G5	04:56:08.47	-21:59:02.61	23.7	-18.4	0.5337	0.8	9.2	58.8	+45
G6	04:56:09.49	-21:59:15.14	23.0	-19.1	0.5373	0.8	10.7	69.0	+749
G7	04:56:10.00	-21:59:12.20	22.4	-19.7	0.5408	0.5	16.7	107.9	+1433
G8	04:56:10.00	-21:59:13.54	23.5	-18.6	0.5410	0.6	17.0	109.8	+1473
G9	04:56:07.93	-21:59:18.11	23.9	-18.2	0.5411	0.2	17.1	110.6	+1492
G10	04:56:10.10	-21:59:09.60	23.4	-18.7	0.5398	0.7	17.9	115.7	+1238
G11	04:56:09.21	-21:58:50.90	22.1	-20.0	0.5328	0.9	18.8	120.2	-130
G12	04:56:08.72	-21:58:46.62	23.3	-18.8	0.5298	0.7	22.6	144.6	-716
G13	04:56:10.66	-21:59:10.08	24.0	-18.1	0.5331	0.4	26.5	169.7	-71
G14	04:56:10.54	-21:58:49.26	23.8	-18.3	0.5338	0.7	31.6	202.8	+65
G15	04:56:10.96	-21:59:20.44	23.6	-18.5	0.5386	0.6	32.9	211.8	+1003
G16	04:56:10.81	-21:59:35.43	24.0	-18.1	0.5369	0.3	38.9	250.3	+671

Notes.^a Right ascension.^b Declination.^c Apparent *HST* WFPC2+F702W magnitude, in AB magnitudes.^d Absolute *g*-band magnitude, in AB magnitudes.^e Best-fit redshift.^f Rest-frame *u-g* color, measured in matched isophotal apertures determined by **Source Extractor**.^g Projected angular distance from the quasar, with units of arcsec.^h Projected physical distance from the quasar, with units of pkpc.ⁱ LOS velocity from the quasar, with units of km s⁻¹.**Table 2.** Summary of Nebulae in the Field of PKS0454–22 at $z \approx z_{\text{QSO}}$.

ID	Area ^a (pkpc ²)	[O II] ^b (erg s ⁻¹)	H β ^c (erg s ⁻¹)	[O III] ^d (erg s ⁻¹)	$r_{[\text{O II}]}$ ^e	$r_{[\text{O III}]}$ ^f	Δv ^g (km s ⁻¹)	σ ^h (km s ⁻¹)	Associated Galaxies
N1	3100	3.0×10^{43}	8.8×10^{42}	7.2×10^{43}	1.05 ± 0.05	0.012 ± 0.003	+140	140	Host, G1, G2
N2	3200	1.7×10^{43}	5.2×10^{42}	5.5×10^{43}	1.36 ± 0.05	0.014 ± 0.002	+1330	120	G8, G7, G10
N3	400	7.9×10^{41}	2.2×10^{41}	1.8×10^{42}	1.41 ± 0.23	0.048 ± 0.029	+550	50	none

Notes.^a Area, with units of pkpc².^b Total line luminosity in [O II] $\lambda\lambda 3727 + 3729$, with units of erg s⁻¹.^c Total line luminosity in H β , with units of erg s⁻¹.^d Total line luminosity in [O III] $\lambda\lambda 4959 + 5008$, with units of erg s⁻¹.^e Line ratio of [O II] $\lambda 3729$ to [O II] $\lambda 3727$, with errors.^f Line ratio of [O III] $\lambda 4363$ to [O III] $\lambda 5008$, with errors.^g LOS velocity relative to the quasar, with units of km s⁻¹.^h LOS velocity dispersion, with units of km s⁻¹.

the closest spectral extraction to the quasar considered here. To account for this blue emission wing, we modified our spectral modeling technique by fitting two sets of Gaussian line components with tied width and velocity as described previously, finding a best fit of $\Delta v \approx 196$ km s⁻¹ from the quasar and $\sigma \approx 116$ km s⁻¹. This sort of feature is prevalent among luminous quasars (Liu et al. 2013a,b), and is typically associated with outflows.

4 DISCUSSION**4.1 Origin of the Nebular Gas**

The two largest and most luminous nebulae (N1 and N2) are kinematically and morphologically coincident with interacting galaxies in the field of PKS0454–22, as shown in Figure 4. In particular, N1 spatially and kinematically surrounds the interacting galaxy triple Host/G1/G2 while N2 spatially and kinematically surrounds the interacting galaxy triple G8/G7/G10. The kinematic and morphological correspondence with interacting galaxies, the narrow internal velocity dispersions exhibited by these nebulae ($\sigma \approx 110$ – 140 km s⁻¹),

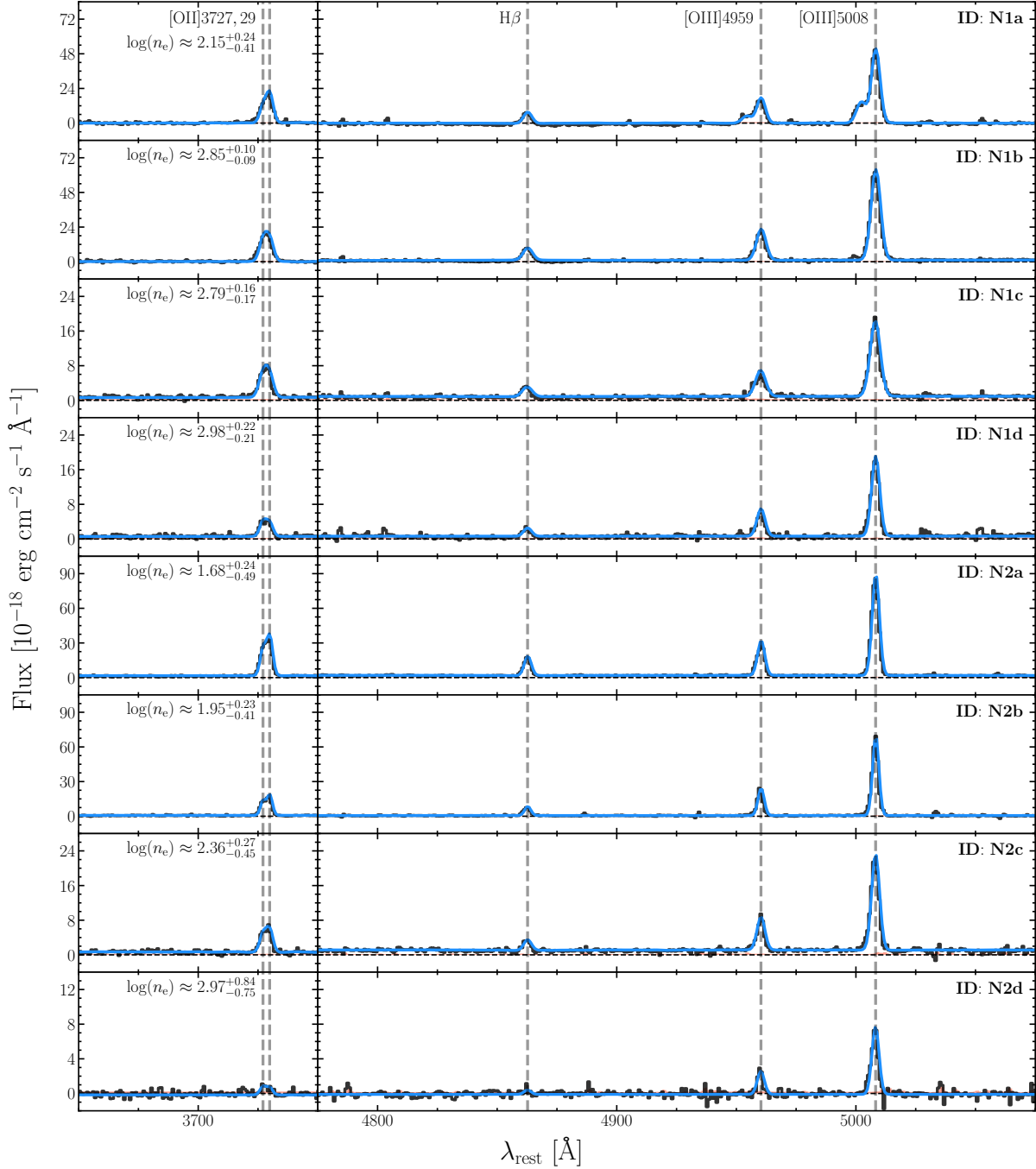


Figure 5. Examples of co-added nebular spectra and best-fitting spectral models for various regions within each of the 3 kinematically and morphologically distinct, ionized nebulae (N1, N2, and N3). The MUSE spectrum is shown by a solid line in black with errors shown by a filled area in red, while the best-fit spectral model is shown by a solid line in blue. Nebula labels are in the upper-right corner of each panel.

and the high densities of these nebulae ($n_e \approx 60 - 800 \text{ cm}^{-3}$) are most consistent with stripped ISM resulting from ongoing interactions (Poggianti et al. 2017; Bellhouse et al. 2017).

Unlike the other nebulae, N3 is a narrow gas cloud extending $d \approx 70 - 95 \text{ pkpc}$ from the quasar with a major axis angular offset of ≈ 30 degrees, a width of $\lesssim 10 \text{ pkpc}$, and a LOS velocity of $\Delta v \approx +550 \text{ km s}^{-1}$ from the quasar, as shown in the bottom-left panel of Figure 4. N3 is the faintest of the

nebulae with the lowest surface brightness, the lowest internal velocity dispersion, and the lowest ionization. Additionally, it is not associated with any nearby continuum sources detected in the *HST* or MUSE images, which is complete at $m_{F702W} \approx 25 - 26$. The morphology, low surface brightness, calm kinematics, low ionization state, and lack of any associated galaxies all suggest that this is a cool gas structure in the IGrM (Borthakur et al. 2010; Steidel et al. 2010).

4.2 Origin of the Nebular Photoionization

From Table 2 and Figure 5, we see that the nebulae exhibit high ionization states with mean $\log([\text{O III}]\lambda 5008/[\text{O II}]\lambda\lambda 3727, 3729) \approx 0.3 - 0.6$ and mean $\log([\text{O III}]\lambda 5008/\text{H}\beta) \approx 0.9 - 1.3$. Such high ionization states can be produced with photoionization by a quasar (Groves et al. 2004a) or fast shocks (Allen et al. 2008), but cannot be produced with photoionization by stars, even from a very young stellar population (Morisset et al. 2014).

To better quantify the ionization properties of the gas, we compare various line ratios ($[\text{O III}]\lambda 5008/[\text{O II}]\lambda\lambda 3727, 3729$, $[\text{O III}]\lambda 5008/\text{H}\beta$, $[\text{O III}]\lambda 4363/[\text{O III}]\lambda 5008$, $[\text{Ne V}]\lambda 3427/[\text{Ne III}]\lambda 3869$) for the brightest nebular regions with dusty radiation pressure-dominated quasar models, calculated with MAPPINGS III (Groves et al. 2004a,b) and fully radiative shock models, calculated with MAPPINGS V (Sutherland & Dopita 2017). We also compare various line ratios for the brightest nebular regions with dusty radiation pressure-dominated photoionization models from Cloudy (Ferland et al. 2017). Figure 6 shows these comparisons. We only consider nebular regions with signal-to-noise ratio $S/N > 3$ in each line for this analysis, unless stated otherwise.

For the MAPPINGS III models we utilize the IDL Tool for Emission-line Ratio Analysis (ITERA), which assumes a simple power law to represent the spectrum of the ionizing source, abundances similar to that deduced by Allen et al. (1998), and an electron density motivated by observations (Groves & Allen 2010). For the MAPPINGS V models we utilize the Mexican Million Models dataBase-shocks (3MdBs), which assumes a shock plus precursor model, abundances from Allen et al. (2008), and an electron density motivated by observations (Alarie & Morisset 2019). For the Cloudy models we assume many different incident radiation field shapes, chemical compositions, and density laws. The MAPPINGS III model grids span various power law slopes (α) and ionization parameters (U) while the MAPPINGS V model grids span various shock velocities (v_{shock}) and magnetic field strengths (B). The ionization parameter U is defined here as the dimensionless ratio of hydrogen-ionizing photons to total-hydrogen densities.

We use the $[\text{O II}]\lambda 3729/[\text{O II}]\lambda 3727$ line ratio averaged over each nebula to measure the electron density (n_e) and the $[\text{O III}]\lambda 4363/[\text{O III}]\lambda 5008$ line ratio averaged over each nebula to measure the electron temperature (T_e) following the prescription of Osterbrock & Ferland (2006) as implemented in PyNeb (Luridiana et al. 2015). These line ratios are given in Table 2 and imply values of $\log(n_e/\text{cm}^{-3}) \approx 2.82^{+0.08}_{-0.05}$ and $\log(T_e/\text{K}) \approx 4.08^{+0.04}_{-0.05}$ for the nebular regions associated with N1 and $\log(n_e/\text{cm}^{-3}) \approx 2.05^{+0.14}_{-0.25}$ and $\log(T_e/\text{K}) \approx 4.11^{+0.02}_{-0.02}$ for the nebular regions associated with N2, while the errors associated with N3 are too high to accurately measure the electron density or temperature.

We see that our 3 kinematically and morphologically distinct, ionized nebulae exhibit very different galaxy associations, LOS velocities, projected physical distances, and electron density. These different projected physical distances and electron densities necessitate separate photoionization modeling. While N1 and N2 are strongly emitting, allowing for significant detection in many of the emission lines used for this analysis and accurate measurements of elec-

tron density and temperature, N3 is weakly emitting with no significant detection in many of the emission lines used for this analysis and no accurate measurements of electron density and temperature. Thus, we will only consider N1 and N2 for subsequent photoionization analysis. In Figure 6, nebular regions associated with N1 are shown by the red points, while nebular regions associated with N2 are shown by the blue points.

4.2.1 Nebula 1: Close to the Quasar

For the nebular regions associated with N1, we find that the MAPPINGS III quasar model with solar metallicity, $-3.3 \leq \log(U) \leq -2.3$, and $-2.0 \leq \alpha \leq -1.2$ is consistent with the observed strong line ratios, as shown by the red points in the left column of Figure 6. The range in ionization parameter shown is the full physically realizable range based on the observed luminosity of the quasar ($L_{\text{bol}} \approx 10^{47} \text{ erg s}^{-1}$), the measured electron densities of these nebulae ($\log(n_e/\text{cm}^{-3}) \approx 2.82^{+0.08}_{-0.05}$), and the various projected distances of these nebulae ($d \approx 10 - 75 \text{ pkpc}$). While we are able to reproduce the observed strong line ratios ($[\text{O III}]\lambda 5008/[\text{O II}]\lambda\lambda 3727, 3729$ and $[\text{O III}]\lambda 5008/\text{H}\beta$) and one of the temperature sensitive weak line ratio ($[\text{O III}]\lambda 4363/[\text{O III}]\lambda 5008$) with this model, we are unable to reproduce the ionization sensitive weak line ratio ($[\text{Ne V}]\lambda 3427/[\text{Ne III}]\lambda 3869$) with this model.

On the other hand, the MAPPINGS V shock model with solar metallicity, $200 \text{ km s}^{-1} \leq v_{\text{shock}} \leq 600 \text{ km s}^{-1}$, and $1.0 \mu\text{G} \leq B \leq 100.0 \mu\text{G}$ are inconsistent with the measured strong and weak line ratios, as shown by the red points in the right column of Figure 6.

For the nebular regions considered here, the line ratios $[\text{O III}]\lambda 5008/[\text{O II}]\lambda\lambda 3727, 3729$ are generally anti-correlated with the projected distance from the quasar, consistent with gas in the quasar host group that is photoionized by the quasar. Additionally, the internal velocity dispersion are low with $\sigma \approx 140 \text{ km s}^{-1}$, which disfavors the shock scenario since it requires relatively fast shocks of $v_{\text{shock}} \approx 200 - 600 \text{ km s}^{-1}$. Based on this and the red points of Figure 6, it seems that the nebular regions associated with N1 are predominantly being photoionized by the quasar. To try and reproduce the other observed weak line ratio, we compared the ionization properties of the gas with dusty radiation pressure-dominated photoionization models from Cloudy (Ferland et al. 2017) assuming many different incident radiation field shapes, chemical compositions, and densities. With the additional model parameters explored by this technique, we were able to reproduce some of the observed line ratios ($[\text{O III}]\lambda 5008/[\text{O II}]\lambda\lambda 3727, 3729$, $[\text{O III}]\lambda 5008/\text{H}\beta$, and $[\text{O III}]\lambda 4363/[\text{O III}]\lambda 5008$), but not all ($[\text{Ne V}]\lambda 3427/[\text{Ne III}]\lambda 3869$). In future work, we will explore additional possibilities including log-normal density distributions (Cantalupo et al. 2019) which may explain the more highly ionized emission. Nevertheless, based on the proximity to the quasar, kinematics, strong-line ratios, anti-correlation between $[\text{O III}]\lambda 5008/[\text{O II}]\lambda\lambda 3727, 3729$, and projected distance from the quasar, UV photons from the quasar is the most likely explanation for the ionization of this gas.

4.2.2 Nebula 2: Far from the Quasar

For the nebular regions associated with N2, we find that the MAPPINGS III quasar model with solar metallicity, $-4.0 \leq \log(U) \leq -3.0$, and $-2.0 \leq \alpha \leq -1.2$ is inconsistent with the observed line ratios, as shown by the blue points in the left column of Figure 6. The range in ionization parameter quoted here is the full physically realizable range based on the observed luminosity of the quasar ($L_{\text{bol}} \approx 10^{47} \text{ erg s}^{-1}$), the measured electron densities of these nebulae ($\log(n_e/\text{cm}^{-3}) \approx 2.05^{+0.14}_{-0.25}$), and the various projected distances of these nebulae ($d \approx 75 - 150 \text{ pkpc}$). We are unable to reproduce either the observed strong line ratios or the observed weak line ratios with this model, given the full physically realizable range in ionization parameter. Furthermore, we compared the ionization properties of the gas with dusty radiation pressure-dominated photoionization models from Cloudy (Ferland et al. 2017) assuming many different incident radiation field shapes, chemical compositions, and densities. We find that these conclusions about the origin of the nebular photoionization still hold, and we do not gain any more information about the gas, even with these additional free parameters. In order to explain the observed line ratios, the quasar would need to have been ≈ 10 times brighter in the past, with $L_{\text{bol}} \approx 10^{48} \text{ erg s}^{-1}$ roughly 0.3 Myr ago.

We find that the MAPPINGS V shock model with solar metallicity, $200 \text{ km s}^{-1} \leq v_{\text{shock}} \leq 600 \text{ km s}^{-1}$, and $1.0 \mu\text{G} \leq B \leq 100.0 \mu\text{G}$ to be consistent with the measured strong and weak line diagnostics, as shown by the blue points in the right column of Figure 6. While the nebular regions considered here have low internal velocity dispersions with $\sigma \approx 40 - 140 \text{ km s}^{-1}$, they are likely moving through the intragroup medium (IGrM) of the quasar host with $+500 \text{ km s}^{-1} \lesssim \Delta v \lesssim +1500 \text{ km s}^{-1}$, comparable to the required shock velocities from the models. Based on this and Figure 6, it seems that the nebular regions associated with N2 are predominantly being photoionized by fast shocks, which could arise from the interaction between nebulae and the hot IGrM of the quasar host group.

5 SUMMARY AND CONCLUSIONS

We reported wide-field optical integral field spectroscopy of PKS0454–22, one of the most luminous quasars in the $z < 1$ Universe, with MUSE at the VLT. The wide field of view, high spatial sampling, and broad wavelength coverage of MUSE allowed us to thoroughly study the gaseous and group environment hosting PKS0454–22 using a spatially resolved analysis of the given morphologies, kinematics, and nebular photoionization properties. Our findings can be summarized as follows.

- (i) We found that PKS0454–22 sits in an overdense region of galaxies comprised of two kinematic and spatial groupings. This can be explained if perhaps a smaller group of 5 galaxies at $\Delta v \approx 1320 \text{ km s}^{-1}$ and $\sigma \approx 190 \text{ km s}^{-1}$ is interacting with or infalling into the more massive quasar host group with 12 galaxies at $\Delta v \approx 70 \text{ km s}^{-1}$ and with $\sigma \approx 370 \text{ km s}^{-1}$.
- (ii) From these galaxies, we found an interacting galaxy triple (Host/G1/G2, see Figure 1) with a projected separation of 37.4 pkpc and an interacting galaxy triple

(G8/G7/G10, see Figure 1) with a projected separation of 25.7 pkpc based on the galaxy morphologies, projected separations, and relative velocities. All of these interacting galaxies appear dominated by intermediate to old characteristic stellar populations.

(iii) We identified three kinematically and morphologically distinct, ionized nebulae emitting strongly in [O II], H β , and [O III] on scales of 10 – 150 pkpc and at LOS velocities of $\Delta v \approx -500$ to $+1500 \text{ km s}^{-1}$ from the quasar. In particular, the first is morphologically coincident with the interacting galaxy pair (N1, see Figure 4), the second is morphologically coincident with the interacting galaxy triple (N2, see Figure 4), and the third is not morphologically coincident with any galaxies (N3, see Figure 4).

(iv) We found that the two largest and most luminous nebulae (N1 and N2) are most consistent with stripped ISM resulting from ongoing interactions, based on their kinematic and morphological correspondence with interacting galaxies, their narrow internal velocity dispersions, and their high densities. On the other hand, we found that N3 is most likely a cool gas structure in the intragroup medium based on its morphology, low surface brightness, calm kinematics, low ionization state, and lack of any associated galaxies.

(v) To better understand the two largest and most luminous nebulae (N1 and N2), we compared optical line ratios for some of the brightest nebular regions with dusty radiation pressure-dominated quasar photoionization models and radiative shock models to better quantify the ionization properties of the gas. We found that the nebular regions associated with N1 are most likely being predominantly photoionized by the quasar. We found that the nebular regions associated with N2 are most likely being predominantly photoionized by fast shocks, which could arise from the interaction between nebulae and the hot intragroup medium of the quasar host group.

Using wide-field optical integral field spectroscopy, we were able to simultaneously survey the galactic and gaseous environment around PKS0454–22, allowing both a sensitive search for extended line-emitting nebulae and joint studies of their morphologies and kinematics in the context of those of nearby galaxies. The presence of these spatially extended ionized nebulae in the host group of one of the most luminous quasars in the $z < 1$ Universe provide evidence supporting interaction related triggering of quasars. These interactions also drive large quantities of interstellar medium to the circumgalactic medium, producing cool gas structures on halo scales. This demonstrates the power of integral field spectroscopy when combined with photoionization from active galactic nuclei and shocks for revealing typically neutral gas. While focusing on a single system such as PKS0454–22 is beneficial, we need further analysis on other systems and robust statistics to fully understand the importance of galaxy environment and interactions in fueling galaxy and black hole growth.

ACKNOWLEDGEMENTS

REFERENCES

- Alarie A., Morisset C., 2019, *Revista Mexicana de Astronomía y Astrofísica*, 55, 377

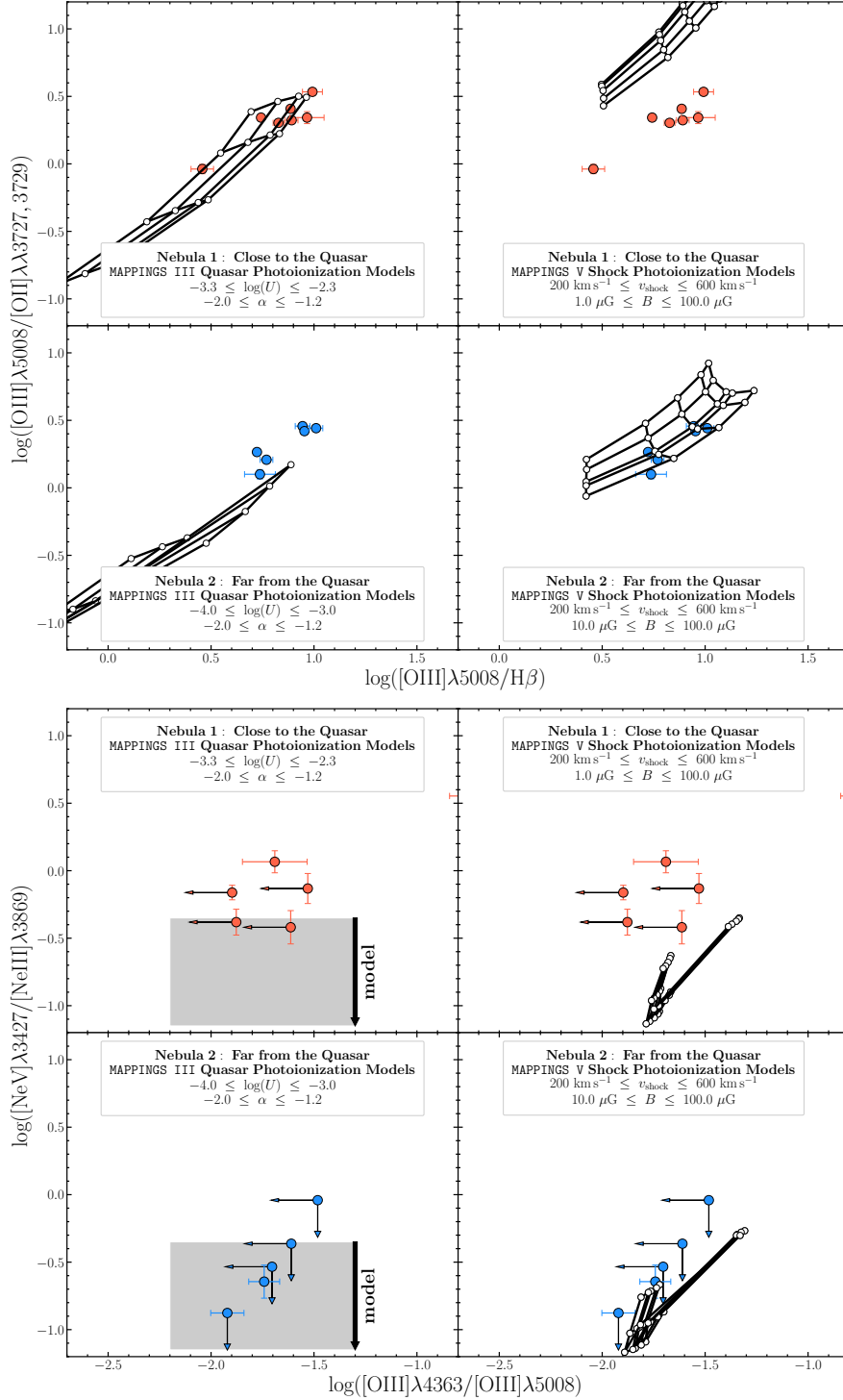


Figure 6. The emission line diagnostic diagrams $\log([O\ III]\lambda 5008/[O\ II]\lambda 3727, 3729)$ vs. $\log([O\ III]\lambda 5008/H\beta)$ and $\log([Ne\ V]\lambda 3427/[Ne\ III]\lambda 3869)$ vs. $\log([O\ III]\lambda 4363/[O\ III]\lambda 5008)$ for the various extended line-emitting nebulae. Nebular regions associated with N1 are shown by the red points and labeled in the legend, while nebular regions associated with N2 are shown by the blue points and labeled in the legend. For nebulae with S/N > 3 in each of the given lines, we plot points with error bars. Otherwise, we plot 3 σ upper limits. We compare these line ratios with dusty radiation pressure-dominated quasar models calculated with MAPPINGS III (Groves et al. 2004a,b) in the left column and fully radiative shock models calculated with MAPPINGS V (Sutherland et al. 2018) in the right column. For the MAPPINGS III models we assume a simple power law to represent the spectrum of the ionizing source, abundances similar to that deduced by Allen et al. (1998), $n_e \approx 1000\text{ cm}^{-3}$ for the nebular regions associated with N1, and $n_e \approx 100\text{ cm}^{-3}$ for the nebular regions associated with N2. For the MAPPINGS V models we assume a shock plus precursor model, abundances similar to that deduced by Allen et al. (2008), $n_e \approx 1000\text{ cm}^{-3}$ for the nebular regions associated with N1, and $n_e \approx 100\text{ cm}^{-3}$ for the nebular regions associated with N2. The MAPPINGS III model grids span various power law slopes (α) and ionization parameters (U) while the MAPPINGS V model grids span various shock velocities (v_{shock}) and magnetic field strengths (B), as shown in the legend.

- Allen C., Carigi L., Peimbert M., 1998, [\apj](#), 494, 247
- Allen M. G., Groves B. A., Dopita M. A., Sutherland R. S., Kewley L. J., 2008, [The Astrophysical Journal Supplement Series](#), 178, 20
- Bacon R., et al., 2010, in Society of Photo-Optical Instrumentation Engineers (SPIE) Conference Series, Vol. 7735, Proceedings of the SPIE, Volume 7735, id. 773508 (2010).. p. 773508, [doi:10.1117/12.856027](#)
- Bacon R., et al., 2014, [The Messenger](#), 157, 13
- Bahcall N. A., Chokshi A., 1991, [ApJ](#), 380, L9
- Bahcall J. N., Kirhakos S., Saxe D. H., Schneider D. P., 1997, [ApJ](#), 479, 642
- Barnes J. E., Hernquist L. E., 1991, [ApJ](#), 370, L65
- Barnes J. E., Hernquist L., 1996, [ApJ](#), 471, 115
- Bellhouse C., et al., 2017, [The Astrophysical Journal](#), 844, 49
- Bertin E., Arnouts S., 1996, [\aaps](#), 117, 393
- Blanton M. R., Roweis S., 2007, [The Astronomical Journal](#), 133, 734
- Bolton A. S., et al., 2012, [The Astronomical Journal](#), 144, 144
- Borisova E., et al., 2016, [ApJ](#), 831, 39
- Boroson T. A., Green R. F., 1992, [The Astrophysical Journal Supplement Series](#), 80, 109
- Borthakur S., Yun M. S., Verdes-Montenegro L., 2010, [ApJ](#), 710, 385
- Bruzual G., Charlot S., 2003, [Monthly Notices of the Royal Astronomical Society](#), 344, 1000
- Cantalupo S., Arrigoni-Battaia F., Prochaska J. X., Hennawi J. F., Madau P., 2014, [Nature](#), 506, 63
- Cantalupo S., et al., 2019, [MNRAS](#), 483, 5188
- Chen H.-W., Boettcher E., Johnson S. D., Zahedy F. S., Rudie G. C., Cooksey K. L., Rauch M., Mulchaey J. S., 2019, [The Astrophysical Journal](#), 878, L33
- Di Matteo T., Croft R. A. C., Springel V., Hernquist L., 2003, [ApJ](#), 593, 56
- Duc P.-A., Renaud F., 2013, Tides in Colliding Galaxies. p. 327, [doi:10.1007/978-3-642-32961-6_9](#)
- Epinat B., et al., 2018, [A&A](#), 609, A40
- Ferland G. J., et al., 2017, [Rev. Mex. Astron. Astrofis.](#), 53, 385
- Gebhardt K., et al., 2000, [The Astrophysical Journal](#), 539, L13
- Groves B. A., Allen M. G., 2010, [New Astronomy](#), 15, 614
- Groves B. A., Dopita M. A., Sutherland R. S., 2004a, [The Astrophysical Journal Supplement Series](#), 153, 9
- Groves B. A., Dopita M. A., Sutherland R. S., 2004b, [The Astrophysical Journal Supplement Series](#), 153, 75
- Häring N., Rix H.-W., 2004, [\apjl](#), 604, L89
- Hernquist L., 1989, [Nature](#), 340, 687
- Hickox R. C., et al., 2009, [ApJ](#), 696, 891
- Hopkins P. F., Quataert E., 2010, [MNRAS](#), 407, 1529
- Hopkins P. F., Hernquist L., Cox T. J., Di Matteo T., Robertson B., Springel V., 2006, [The Astrophysical Journal Supplement Series](#), 163, 1
- Hopkins P. F., Hernquist L., Cox T. J., KereÅ D., 2008a, [The Astrophysical Journal Supplement Series](#), 175, 356
- Hopkins P. F., Cox T. J., KereÅ D., Hernquist L., 2008b, [ApJS](#), 175, 390
- Husemann B., SÃ¡nchez S. F., Wisotzki L., Jahnke K., Kupko D., Nugroho D., Schramm M., 2010, [Astronomy and Astrophysics](#), 519, A115
- Husemann B., Wisotzki L., Sánchez S. F., Jahnke K., 2013, [A&A](#), 549, A43
- Husemann B., Bennert V. N., ScharwÃdchter J., Woo J.-H., Choudhury O. S., 2016, [Monthly Notices of the Royal Astronomical Society](#), 455, 1905
- Jahnke K., Macciò A. V., 2011, [ApJ](#), 734, 92
- Johnson S. D., et al., 2018, [The Astrophysical Journal](#), 869, L1
- Kamann S., Wisotzki L., Roth M. M., 2013, [A&A](#), 549, A71
- Kormendy J., Ho L. C., 2013, [Annual Review of Astronomy and Astrophysics](#), 51, 511
- Kormendy J., Richstone D., 1995, [\araa](#), 33, 581
- Liu G., Zakamska N. L., Greene J. E., Nesvadba N. P. H., Liu X., 2013a, [MNRAS](#), 430, 2327
- Liu G., Zakamska N. L., Greene J. E., Nesvadba N. P. H., Liu X., 2013b, [MNRAS](#), 436, 2576
- Luridiana V., Morisset C., Shaw R. A., 2015, [Astronomy & Astrophysics](#), 573, A42
- Martini P., 2004, in Ho L. C., ed., Coevolution of Black Holes and Galaxies. p. 169 ([arXiv:astro-ph/0304009](#))
- McLure R. J., Dunlop J. S., 2002, [Monthly Notices of the Royal Astronomical Society](#), 331, 795
- Morisset C., Delgado-Inglada G., Flores-Fajardo N., 2014, [arXiv:1412.5349 \[astro-ph\]](#)
- Myers A. D., Brunner R. J., Nichol R. C., Richards G. T., Schneider D. P., Bahcall N. A., 2007a, [ApJ](#), 658, 85
- Myers A. D., Brunner R. J., Richards G. T., Nichol R. C., Schneider D. P., Bahcall N. A., 2007b, [ApJ](#), 658, 99
- Osterbrock D. E., Ferland G. J., 2006, Astrophysics of gaseous nebulae and active galactic nuclei
- Peng C. Y., 2007, [ApJ](#), 671, 1098
- Peroux C., et al., 2019, [Monthly Notices of the Royal Astronomical Society](#), 485, 1595
- Piqueras L., Conseil S., Shepherd M., Bacon R., Leclercq F., Richard J., 2017, [arXiv:1710.03554 \[astro-ph\]](#)
- Poggianti B. M., et al., 2017, [The Astrophysical Journal](#), 844, 48
- Reid R. I., Kronberg P. P., Perley R. A., 1999, [ApJS](#), 124, 285
- Ren B., Pueyo L., Zhu G. B., Debes J., DuchÃine G., 2018, [The Astrophysical Journal](#), 852, 104
- Richards G. T., et al., 2006, [The Astrophysical Journal Supplement Series](#), 166, 470
- Ross N. P., et al., 2009, [ApJ](#), 697, 1634
- Rupke D. S. N., GÃijltekin K., Veilleux S., 2017, [The Astrophysical Journal](#), 850, 40
- Shen Y., et al., 2007, [AJ](#), 133, 2222
- Smith E. P., Heckman T. M., 1990, [ApJ](#), 348, 38
- Somerville R. S., Davé R., 2015, [Annual Review of Astronomy and Astrophysics](#), 53, 51
- Somerville R. S., Hopkins P. F., Cox T. J., Robertson B. E., Hernquist L., 2008, [MNRAS](#), 391, 481
- Springel V., Di Matteo T., Hernquist L., 2005, [ApJ](#), 620, L79
- Steidel C. C., Erb D. K., Shapley A. E., Pettini M., Reddy N., BogosavljeviÃ M., Rudie G. C., Rakic O., 2010, [The Astrophysical Journal](#), 717, 289
- Stockton A., 1978, [ApJ](#), 223, 747
- Stott J. P., et al., 2020, [arXiv e-prints](#), p. [arXiv:2006.07384](#)
- Strateva I., et al., 2001, [\aj](#), 122, 1861
- Sutherland R. S., Dopita M. A., 2017, [The Astrophysical Journal Supplement Series](#), 229, 34
- Tremaine S., et al., 2002, [The Astrophysical Journal](#), 574, 740
- Vestergaard M., Peterson B. M., 2006a, [The Astrophysical Journal](#), 641, 689
- Vestergaard M., Peterson B. M., 2006b, [ApJ](#), 641, 689
- Vestergaard M., Wilkes B. J., 2001, [The Astrophysical Journal Supplement Series](#), 134, 1
- Weilbacher P. M., Streicher O., Urrutia T., Jarno A., PÃlcontal-Rousset A., Bacon R., BÃhm P., 2012, in Society of Photo-Optical Instrumentation Engineers (SPIE) Conference Series, Vol. 8451, Software and Cyberinfrastructure for Astronomy II. Proceedings of the SPIE, Volume 8451, article id. 84510B, 9 pp. (2012).. p. 84510B, [doi:10.1117/12.925114](#)
- White M., et al., 2012, [MNRAS](#), 424, 933
- Yee H. K. C., Green R. F., 1984, [ApJ](#), 280, 79
- Yee H. K. C., Green R. F., 1987, [ApJ](#), 319, 28
- Yuma S., et al., 2013, [ApJ](#), 779, 53

APPENDIX A: QUASAR LIGHT SUBTRACTION

Luminous quasars significantly outshine their host galaxies, and at intermediate redshifts ($z \gtrsim 0.5$) quasar light can contaminate neighboring galaxies in ground-based data. Mitigating this effect in order to gain useful information about the quasar host galaxy, as well as neighboring galaxies, requires subtraction of the quasar light contamination. Traditional approaches for quasar light subtraction often use an empirical determination of the point-spread function (PSF) based on nearby, bright and unsaturated stars (Kamann et al. 2013). However, not all observations contain a nearby, bright and unsaturated star within the $1.0 \text{ arcmin} \times 1.0 \text{ arcmin}$ field of view (FOV) of MUSE. Alternative approaches for quasar light subtraction at higher redshifts ($z \gtrsim 2$) adopt the quasar as the PSF, with the assumption that there is no contribution from the quasar host galaxy or neighboring galaxies (Cantalupo et al. 2019). However, at lower redshifts ($z \lesssim 1$) where quasar hosts and neighbors contribute non-negligible extended flux, this approach will lead to over-subtraction.

To overcome these challenges, we developed a quasar light subtraction technique that is free of assumptions about the PSF shape. Instead this technique takes advantage of the spectral dimension provided by an integral field spectrograph (IFS) and the fact that galaxy and quasar spectra are distinct (for similar approaches, see Husemann et al. 2013; Rupke et al. 2017). Due to the wavelength dependence of atmospheric seeing, blue light from the quasar is dispersed further away from the quasar centroid than red light. This effect causes the contaminating spectrum from the quasar to be artificially flat (as a function of wavelength) close to the quasar, and artificially steep far from it. Figure A1 demonstrates this effect by comparing co-added quasar spectra extracted in annuli around the quasar, with the spectra becoming steeper for larger annuli. To account for this wavelength dependence, we used non-negative matrix factorization (NMF) (Blanton & Roweis 2007; Ren et al. 2018) to derive two non-orthogonal, non-negative spectral components that can describe the quasar contamination to any spaxel as a linear combination. These two non-orthogonal, non-negative spectral components are defined by performing NMF on quasar-dominated spaxels from a $1.0 \text{ arcsec} \times 1.0 \text{ arcsec}$ aperture centered around the quasar. The first of these components (Q_1 , as shown by the blue line in Figure A1) has a steep spectral slope and approximates quasar contamination to spaxels far from the quasar. The second of these components (Q_2 , as shown by the red line in Figure A1) has a shallow spectral slope and approximates quasar contamination to spaxels close to the quasar. Linear combinations of these two spectral components accurately model quasar light contributions at $r \gtrsim 0.4 \text{ arcsec}$ from the quasar centroid (as shown by the black lines in Figure A1).

To subtract quasar light from the contaminated regions, we modeled each spaxel at $r \lesssim 6 \text{ arcsec}$ from the quasar as a linear combination of Q_1 and Q_2 , as well as two galaxy eigenspectra from the Baryon Oscillation Spectroscopic Survey (BOSS; Bolton et al. 2012), shifted to $z_{\text{QSO}} = 0.5335$ with the strongest emission lines masked. In particular, the spectrum at each location is modeled by Equation A1

$$m(\lambda) = a_1 Q_1(\lambda) + a_2 Q_2(\lambda) + b_1 G_1(\lambda) + b_2 G_2(\lambda) \quad (\text{A1})$$

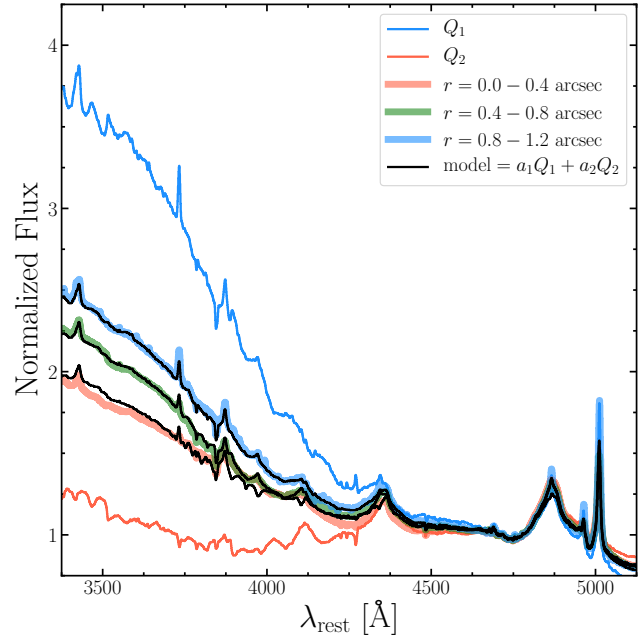


Figure A1. Examples of co-added quasar spectra extracted in annuli and best-fitting spectral models from a linear combination of NMF components. The annuli are centered on the quasar centroid with inner and outer radii specified in the figure legend. Due to the wavelength dependent seeing, the spectra extracted from smaller annuli are artificially shallow while the spectra extracted from larger annuli are artificially steep. To model this effect, we performed NMF on spaxels dominated by the quasar light to define two non-orthogonal, non-negative spectral components (Q_1 and Q_2) which are able to approximate the quasar contribution as a linear combination. To demonstrate the effectiveness of this technique, we fit each annular extracted spectrum with a linear combination of the two non-orthogonal, non-negative spectral components ($a_1 Q_1 + a_2 Q_2$) and overplot the best-fits in black.

where G_1, G_2 are the BOSS galaxy eigenspectra and a_1, a_2, b_1, b_2 are free parameters. We then subtracted the quasar component of the best fit model ($a_1 Q_1 + a_2 Q_2$) from each spaxel, which effectively removes the quasar light contribution at $r \gtrsim 1 \text{ arcsec}$ from the quasar. At $r \lesssim 1 \text{ arcsec}$ from the quasar centroid, the residuals are significant as seen in the right panel of Figure A2, so we mask this area in all measurements presented here. This modeling and subtraction is demonstrated for a nearby galaxy at 5.1 arcsec from the quasar in the middle two panels of Figure A2.

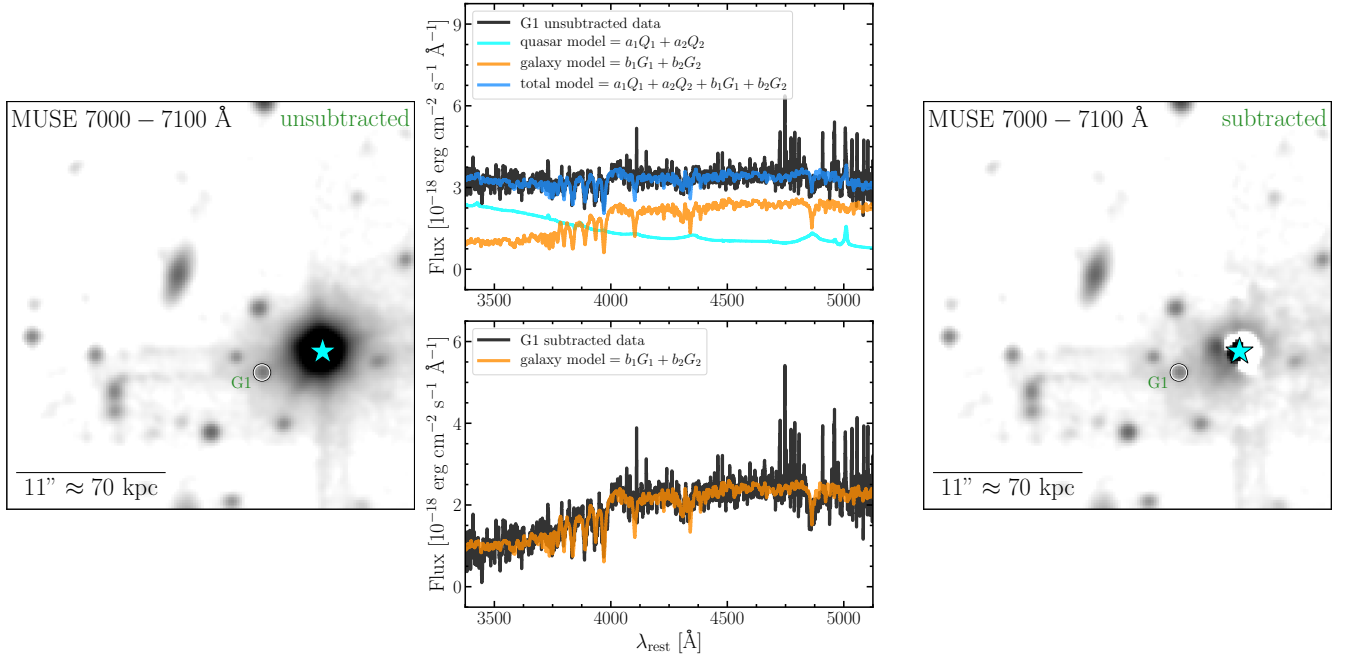


Figure A2. Example of the quasar light subtraction technique. A slice of the unsubtracted MUSE datacube is shown in the left panel while a spectrum from the closest galaxy to the quasar is shown in the top middle panel. We fit the spectrum with a linear combination of galaxy eigenspectra from BOSS, before subtraction. A slice of the subtracted MUSE datacube is shown in the right panel while a spectrum from the closest galaxy to the quasar is shown in the bottom middle panel. We fit the spectrum with a linear combination of galaxy eigenspectra from BOSS, before subtraction. Due to the wavelength dependent seeing, the blue end of the spectrum for this galaxy contains significant contributions from quasar light.